Ionophobicity of carbon sub-nanometer pores enables efficient desalination at high salinity

Author(s):
Zhang, Yuan; Prehal, Christian; Jiang, Huili; Liu, Yang; Feng, Guang; Presser, Volker

Publication date:
2022-01-19

Permanent link:
https://doi.org/10.3929/ethz-b-000527711

Originally published in:
Cell Reports 3(1), https://doi.org/10.1016/j.xcrp.2021.100689

Cell Reports
Physical Science

CellPress
OPEN ACCESS

Article

Ionophobicity of carbon sub-nanometer pores enables efficient desalination at high salinity

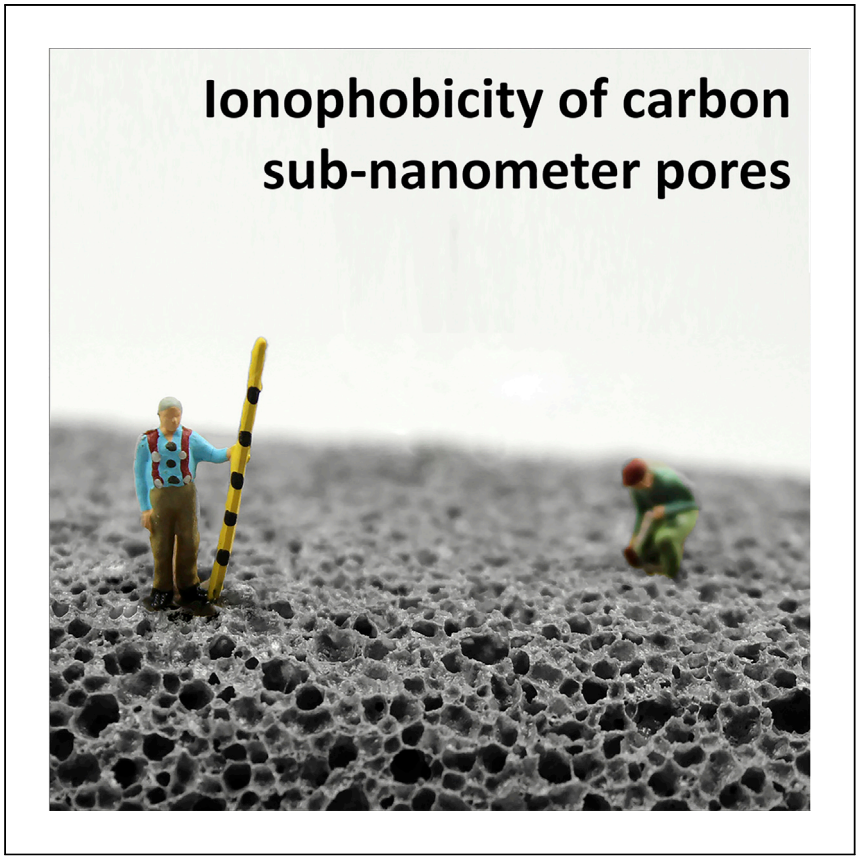

In this work, high capacitive deionization performance is obtained by Zhang et el. using activated carbon with sub-nanometer pore sizes at seawater-level molar strength. Combining experimental results and molecular dynamics simulations shows that desalination performance can be predicted from pore size distribution data.

Yuan Zhang, Christian Prehal, Huili Jiang, Yang Liu, Guang Feng, Volker Presser

gfeng@hust.edu.cn (G.F.)
volker.presser@leibniz-inm.de (V.P.)

Highlights

Sub-nanometer carbon pores can desalinate high-saline water

Predictable desalination performance at high molar strength

Pore size of 0.77 nm shows the highest desalination performance

High charge efficiency and low-cost seawater desalination

Zhang et al., Cell Reports Physical Science 3, 100689
January 19, 2022
https://doi.org/10.1016/j.xcrp.2021.100689

Cell Reports
Physical Science

CellPress
OPEN ACCESS

Article

Ionophobicity of carbon sub-nanometer pores enables efficient desalination at high salinity

Yuan Zhang,[1,2] Christian Prehal,[3] Huili Jiang,[4,5] Yang Liu,[1,2] Guang Feng,[4,5,*] and Volker Presser[1,2,6,7,*]

SUMMARY

Electrochemical seawater desalination has drawn significant attention as an energy-efficient technique to address the global issue of water remediation. Microporous carbons, that is, carbons with pore sizes smaller than 2 nm, are commonly used for capacitive deionization. However, micropores are ineffective for capacitive deionization at high molar strength because of their inability to permselectively uptake ions. In our work, we combine experimental work with molecular dynamics simulation and reveal the ability of sub-nanometer pores (ultramicropores) to effectively desalinate aqueous media at seawater-like molar strength. This is done without any ion-exchange membrane. The desalination capacity in 600 mM reaches 12 mg/g, with a charge efficiency of 94% and high cycling stability over 200 cycles (97% of charge efficiency retention). Using molecular dynamic simulations and providing experimental data, our work makes it possible both to understand and to calculate desalination capacity and charge efficiency at high molar strength as a function of pore size.

INTRODUCTION

With industrialization and human population growth, the lack of fresh water has become a global issue.[1] About 98% of the water in the world is seawater or brackish water; therefore, efficient water desalination techniques are of great importance.[2] Many desalination techniques are applied in practice, such as distillation,[3,4] reverse osmosis,[5,6] and electrodialysis.[7] Electrochemical desalination via capacitive deionization and desalination batteries has the potential for energy-efficient water remediation and tailored ion separation.[8–12] Capacitive deionization (CDI) uses low-cost carbon material electrodes and allows high energy efficiency and a high desalination rate, yet CDI remains restricted to desalination at a low salt concentration, such as found in brackish water.[3,13] The inability of CDI to accomplish desalination at high molar strength is linked to the permselectivity failure and decrease of charge efficiency, where non-permselective ion exchange processes dominate the charge storage mechanism.[14]

CDI cells commonly apply a pair of porous carbon films as the positive and negative electrodes. As salt-containing water flows between the electrode stack, cations and anions are electroadsorbed when the electrodes are being charged; thereby, a stream of desalinated water exits the CDI cell.[15] Ion electrosorption is an interfacial process. Thus, high desalination performance is enabled by electrodes with large pore volume/surface area, such as activated carbons,[16] graphene-based materials,[17] or carbide-derived carbons.[18] Highly microporous carbons provide a large pore volume, but ions in the micropores during the uncharged state present an issue to the application of CDI.[19] During the charging process within the

[1]INM – Leibniz Institute for New Materials, Campus D2 2, 66123 Saarbrücken, Germany

[2]Saarland University, Campus D2 2, 66123 Saarbrücken, Germany

[3]Department of Information Technology and Electrical Engineering, ETH Zürich, Gloriastrasse 35, 8092 Zürich, Switzerland

[4]State Key Laboratory of Coal Combustion, School of Energy and Power Engineering, Huazhong University of Science and Technology (HUST), Wuhan 430074, China

[5]Nano Interface Centre for Energy, School of Energy and Power Engineering, HUST, Wuhan 430074, China

[6]Saarene – Saarland Center for Energy Materials and Sustainability, Campus C4.2, 66123 Saarbrücken, Germany

[7]Lead contact

*Correspondence: gfeng@hust.edu.cn (G.F.), volker.presser@leibniz-inm.de (V.P.)

https://doi.org/10.1016/j.xcrp.2021.100689

electrochemical-potential stability window of water, counter-ions enter the pores to decrease the feed water concentration, and co-ions are ejected from the pore, contributing to a smaller concentration decrease. In solutions with higher salt concentrations, the number of ions initially present inside the pores is higher. During charging, more co-ions are ejected, and fewer counter-ions are adsorbed in the pores, which leads to little concentration change of the feed water.[18,20]

The CDI process can become more permselective when adding one or multiple ion-exchange membranes (MCDI), thereby trapping co-ions and enhancing the desalination metrics.[15] Although most studies have focused on low concentrations,[21,22] our past work applied MCDI in 600 mM NaCl to achieve a desalination capacity of 25 mg/g at a potential range of −1 to +1 V[17]; works such as ours and others show the possibility of applying MCDI for seawater desalination.[10,23] In desalination batteries,[23,24] carbon electrodes are replaced by charge-transfer materials, such as metal oxides,[20] hexacyanoferrates,[25] MXenes,[26] redox-electrolytes,[27] conversion materials,[28,29] or alloying materials.[30] More recent approaches include electrocatalytic processes.[31,32] Although implementing CDI with ion-exchange membranes or charge-transfer materials is an effective way to improve desalination performance, it involves additional material costs and complicates electrode fabrication.

Recently, we have shown that carbon electrodes with tailored sub-nanometer pores show an increased ability to accomplish desalination even at higher molar strength.[33] In this way, without requiring expensive ion-exchange membranes or charge-transfer materials, desalination is accomplished by a low ion population inside small carbon pores in the uncharged state; thereby, less ion exchange (undesirable) and more permselective (desirable) ion uptake is enabled. Yet a robust understanding of the pore size dependency of both charge efficiency and predicted desalination capacity is still missing. To eliminate the belief that CDI is unsuitable for seawater desalination, convincing experimental data are also needed to show robust desalination performance.

Our present work shows the ability of ultramicroporous carbons with sub-nanometer pore sizes to afford a stable and high desalination capacity of 12 mg/g in aqueous 600 mM NaCl at a charge efficiency of 94%. Such performance values are highly comparable with what many microporous carbons deliver at low molar strength (e.g., activated carbon cloth at 5–20 mM: up to 16 mg/g with a charge efficiency of up to 80%–90%).[34,35] As the pore size dispersity of most activated carbons makes it impossible to notice the strong dependency of desalination performance on pore sizes, we have developed a calculation tool that uses pore size distribution data from gas sorption analysis (GSA) and simulation data by applying an interpolation method to predict the desalination performance of a material. With this calculation tool, we vastly advance previous work, such as the "direct prediction of the desalination performance of porous carbon electrodes for capacitive deionization."[36] Our theoretical calculation of desalination performance on the basis of the pore size distribution of carbon materials is extended to 600 mM NaCl and also includes the calculation of charge efficiency in addition to desalination capacity.

Our combined work of experimental desalination and extensive simulation shows that the ability to remove excess salt at high molar strength goes far beyond the "anomalous capacitance increase" in supercapacitors that was explained by the distortion of the solvation shell.[35] The improved desalination performance can

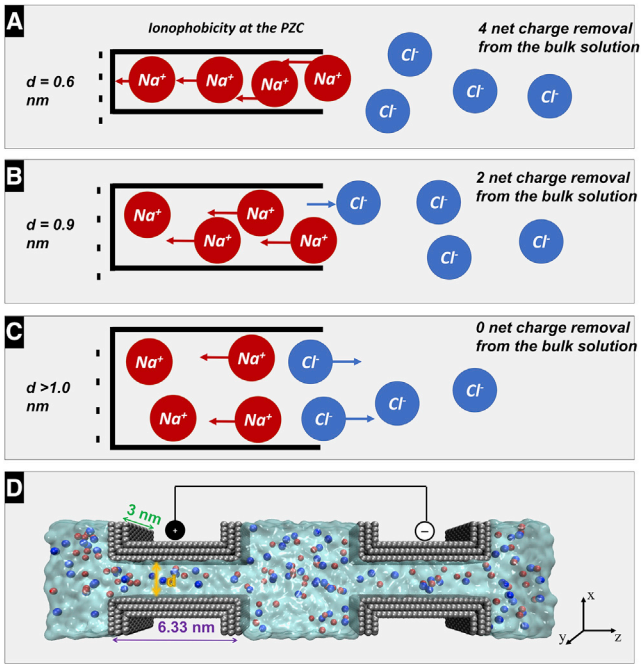

Figure 1. Schematics of possible ion electrosorption mechanisms during the desalination process in high molar salt solutions

(A) Desalination in pore width of 0.6 nm.

(B) Desalination in pore width of 0.9 nm.

(C) Desalination in pore width larger than 1 nm.

(D) Schematic depiction of the molecular dynamics simulation model for ion electrosorption with a pair of micropores during electric polarization.

be explained by the ionophobicity of sub-nanometer carbon nanopores at the uncharged state, which is caused by the dehydration energy barrier for in-pore ion adsorption rather than functional groups and specific adsorption, with important implications for ion separation and energy storage. Molecular dynamics (MD) simulations demonstrate the enhanced desalination capacity by sub-nanometer pore ionophobicity caused by the significant energetic expense of ion desolvation.

RESULTS

Ion electrosorption mechanisms and characterization

Figures 1A and 1B schematically show possible ion electrosorption mechanisms in sub-nanometer pores. The sub-nanometer pore size is comparable with the size of the solvated ion; this confinement will result in incomplete double-layer structures that cannot be explained by the Gouy-Chapman-Stern model.[37,38] The smallest category of pores (0.6 nm; Figure 1A) is ionophobic; that is, the ions are required to desolvate so that there are initially no ions inside the pores at the potential of zero charge (PZC).[39] Ions would only (partially) desolvate and electroadsorb inside the pores upon negative (or positive) polarizations. As the parasitic co-ion expulsion phenomenon is not possible in initially empty 0.6 nm pores, there is more counter-ion uptake compared with larger pores. Figure 1B shows the process in slightly larger pores (0.9 nm). Here, some cations and anions are present inside the pores already at the PZC. When the pore is negatively polarized, some Cl^- ions will be rejected while some Na^+ ions enter the pore. Because of this non-permselective ion

Table 1. Chemical analysis of the different carbon electrode materials ACC-0.59, ACC-0.96, and AC-1.39

	Carbon, mass%	Hydrogen, mass%	Nitrogen, mass%	Oxygen, mass%	Ash content, mass%
ACC-0.59	93.4 ± 0.6	1.0 ± 0.0	0.6 ± 0.0	4.0 ± 0.3	<2
ACC-0.96	95.5 ± 1.0	1.1 ± 0.0	0.7 ± 0.1	4.1 ± 1.0	<2
AC-1.39	96.1 ± 0.4	0.6 ± 0.1	0.3 ± 0.1	2.7 ± 0.1	<2

swapping effect, the net charge uptake is less than in the 0.6 nm pore. For pores larger than 1 nm, the in-pore counter-ion and in-pore co-ion concentrations further increase at the PZC. Co-ion repulsion to the bulk electrolyte would further increase, and the total net ion removal would be close to zero for a high molar bulk electrolyte.[40]

The molecular simulation allows the study of correlations among pore size, ionic strength, and the underlying electrosorption mechanism; thereby, it is possible to quantify the achievable desalination performance. Figure 1D shows a three-dimensional model of the MD simulation schematically. The two pairs of 6.33-nm-long graphite pores contact the 600 mM NaCl bulk aqueous electrolyte and represent the positively and negatively polarized slit pores (where the *d*-value corresponds to the slit pore width). With this model, the dynamic process of ion electroadsorption, ion exchange, and the permselectivity properties of carbon pores can be simulated. Figure S1 depicts the characterization of two activated carbon cloths (ACC) with different average pore sizes (ACC-0.59 and ACC-0.96). The values 0.56 and 0.98 stand for the average pore sizes (in nanometers) according to gas sorption analysis. The pore size difference is caused by different degrees of the activation process. Figures S1A and S1B shows the scanning electron micrographs of the structures of two materials. As seen from the chemical composition provided in Table 1, there are no significant differences between ACC-0.59 and ACC-0.96. The non-carbon mass content for all materials is between 4 mass% and 7 mass%. For ACC-0.59 and ACC-0.96, the functional groups are dominated by acidic groups such as carbonyl and carboxylic groups.[41]

Figures S1C and S1D show the gas sorption isotherm and pore size distribution of the two materials at 87 K (data adapted from Bi et al.[16]). The analyzed pore structure data are shown in Table 2. Compared with ACC-0.59, ACC-0.96 is more activated and has more interpore volumes, higher pore volume, and a larger average pore size compared with ACC-0.59.

Experimental desalination performance

Desalination performance was evaluated by applying ACC-0.59 and ACC-0.96 activated carbon cloth electrodes. Using the same desalination parameters (i.e., flow rate, specific current, galvanostatic potential holding time, and electrode thickness), we quantified the desalination performance of the different electrode materials in 5, 20, and 600 mM NaCl aqueous electrolytes. Figures 2A and 2B shows the effluent concentration profile normalized by the surface area of carbon materials during a galvanostatic charging and discharging cycle using ACC-0.59 and ACC-0.96 in NaCl solutions with different concentrations. For ACC-0.59, the CDI cell shows the most significant concentration change in the 600 mM NaCl solution. As the concentration decreases to 20 and 5 mM, the amplitude is significantly smaller. This indicates that the ionic strength of the electrolyte has a significant influence on the ion electrosorption process in ACC-0.59. For ACC-0.96, on the contrary (Figure 2B),

Table 2. Gas sorption analysis with nitrogen gas at −196°C for ACC-0.59,[16] ACC-0.96, YP-80F (AC-1.39) activated carbon and titanium carbide-derived carbon (CDC-0.57) using the quenched solid density functional theory (QSDFT) and the Brunauer-Emmett-Teller theory (BET)

	SSA BET, m^2/g	SSA DFT, m^2/g	DFT total pore volume, cm^3/g	Average pore size d_{50}, nm
ACC-0.59	916	1032	0.34	0.59
ACC-0.96	2209	1940	0.89	0.96
AC-1.39	2598	1631	1.03	1.39
CDC-0.57	1056	1268	0.40	0.57

Average pore size refers to the volume-normalized value d_{50}. SSA, specific surface area.

the amplitude of concentration change decreases as the ionic strength of the electrolyte increases. When comparing the two types of electrodes in 600 mM molarity, ACC-0.59 shows a much higher concentration change amplitude than ACC-0.96. ACC-0.59 and ACC-0.96 in 600 mM NaCl show different desalination abilities, although ACC-0.96 has a larger average pore size that is beneficial for ion transportation, and ACC-0.59 with an average pore size smaller than the solvated ion sizes shows significantly higher ion removal ability. The comparison between ACC-0.59 and ACC-0.96 in different molarities is provided in Figure S2A. It shows that ACC-0.59 with a smaller average pore size has more efficient desalination ability in 600 mM solution under the same processing condition compared with ACC-0.96.

In Figure 2C, the desalination capacities and charge efficiencies are compared. For ACC-0.59, the desalination capacity and charge efficiency are both low at 5 mM molarity. As the electrolyte concentration increases to 20 mM, the desalination capacity and charge efficiencies significantly improve. In 600 mM NaCl electrolytes, the desalination capacity reaches 12 mg/g, and the charge efficiency is 94%, which are the highest value found in this study. To the best of our knowledge, it is also by far the highest performance of carbon materials in 600 mM high molar strength without an ion-exchange membrane because of its high ion permselectivity that results in higher charge efficiency in sub-nanometer pores.

To prove the pore size effect on water desalination for the carbon materials with different morphology and pore curvatures, the desalination performance in 600 mM NaCl of commercially available activated carbon (YP-80F, Kuraray; abbreviated as AC-1.39)[42–44] and titanium carbide-derived carbon (TiC-CDC; abbreviated as CDC-0.57)[3,18,45] is provided in Figure S2B. AC-1.39 has more phenolic functional groups, while CDC-0.57 has more Cl^--containing species.[46] The gas sorption data for these carbon materials are provided in Table 2. Although the activated carbon has an average pore size of 1.39 nm (pore volume 1.03 cm^3/g), carbide-derived carbon has a much smaller average pore size of only 0.57 nm (pore volume 0.40 cm^3/g). Thus, CDC-0.57 and ACC-0.59 are very similar, but the latter has a much sharper pore size distribution. Accordingly, we see CDC-0.57 has a slightly lower desalination capacity (10 mg/g) and charge efficiency (74%) compared with ACC-0.59 (12 mg/g and 94%). These data show that the importance of sub-nanometer pores for the CDI process at high molar strength is not limited to activated carbon cloth. Also, in agreement with the lowered permselectivity of larger micropores, AC-1.39 is not suitable for CDI at 600 mM molar strength.

When the average pore size of the carbon material increases to about 1.0 nm (ACC-0.96), the electrode's permselectivity is less pronounced. Thus, the charge efficiency

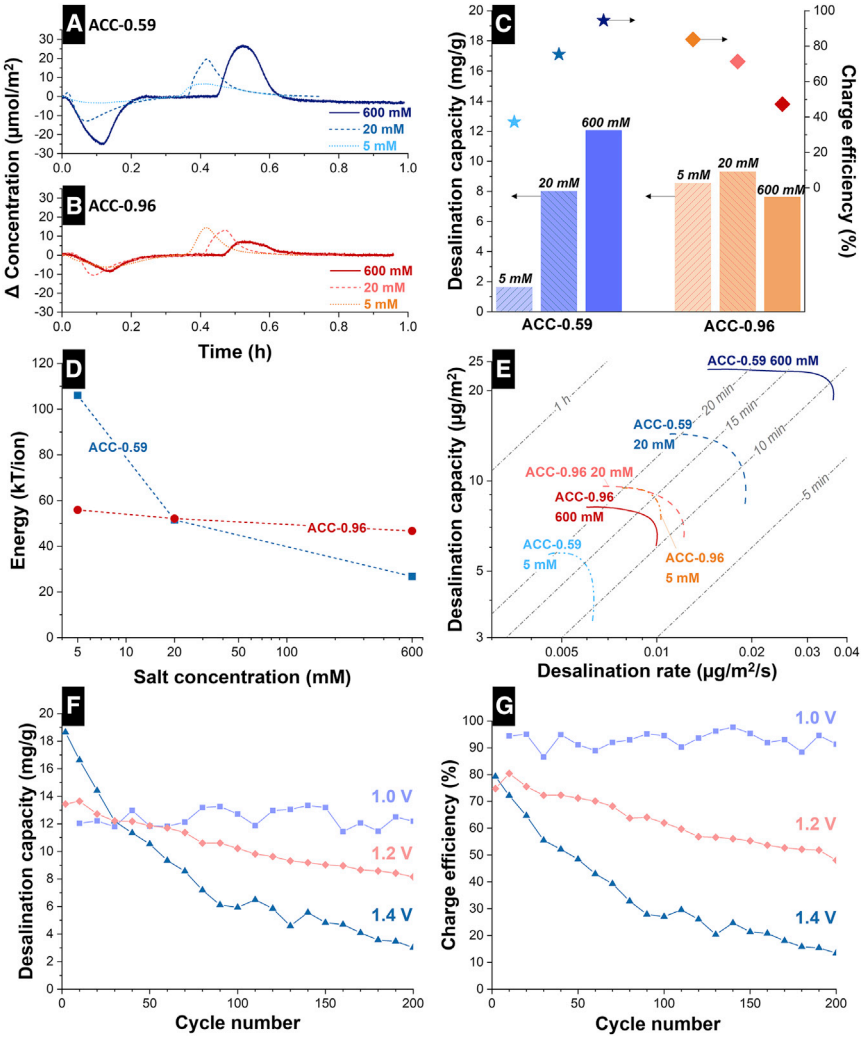

Figure 2. Desalination performance of ACC-0.59 and ACC-0.96 in different concentration of NaCl aqueous solutions

(A) Concentration variation of ACC-0.59 electrode in different molar strength. Galvanosatitic charging/discharging was used with a specific current of 0.1 A/g. A 20 min potential holding period was used.

(B) Concentration variation of ACC-0.96 electrode in different molar strength.

(C) Desalination capacity and charge efficiency of both materials in different molar strength.

(D) Energy consumption of the two materials in different molarities.

(E) Kim-Yoon plot for the two materials in different molarities.

(F and G) Desalination capacity (F) and (G) charge efficiency for ACC-0.59 under 1, 1.2, and 1.4 V throughout 200 cycles.

of the electrode in different electrolytes decreases as the molarity increases. This phenomenon is caused by the increased ion number in the micropores when the cell is not charged, which results in stronger ion swapping under polarization. The desalination capacity of ACC-0.96 in 5 mM NaCl solution is slightly higher than that in ACC-0.59. Under low ionic strength, counter-ion adsorption is generally more dominant than co-ion exclusion, as the in-pore ion concentration at the PZC is low.[42] Therefore reasonable desalination capacities are possible in all carbons. Contrary to the 600 mM solution, there is no enhanced uptake of counter-ions,

because of the ionophobicity in ACC-059. A further experimental factor is the slow ion diffusion in ACC-0.59 with 5 mM NaCl. Within the 20 min holding time, ACC-0.59 in 5 mM NaCl did not reach the maximum ion uptake capacity. The ion diffusion resistivity for smaller pores is higher than that in larger pores; because of the stronger ion diffusion ability in larger pores, ACC-0.96 shows higher desalination abilities in 5 mM NaCl.[43] Compared with ACC-0.59, the desalination capacity of ACC-0.96 is reasonably constant for different salt concentrations, with a maximum value for the 20 mM electrolyte.

The energy consumption of the desalination process per removed ion at different ionic strengths is given in Figure 2D. At the high molarity of 600 mM, ACC-0.96 shows higher energy consumption than ACC-0.59 because of the weakened permselectivity that causes ions with opposite charges to be exchanged in the pores. At 5 mM concentration, the energy consumption of ACC-0.96 is lower than ACC-0.59 because of less significant or no desolvation of the ions upon entering the pore of the former.

The desalination Ragone plot (also known as the Kim-Yoon plot) is shown in Figure 2E. Among all studied concentrations, ACC-0.59 in 600 mM offers the highest desalination capacity and desalination rates. As the salt concentration decreases, the performance of ACC-0.59 goes down. ACC-0.96 has the lowest desalination capacity and rate in the 600 mM electrolyte. In the 5 and 20 mM electrolytes, the desalination rate in the 20 mM NaCl electrolyte is slightly higher. For an electrochemical desalination process, the charging/discharging time should be neither so short that the material is not fully charged/discharged nor so long that the desalination process is inefficient. Figure 2E indicates suitable holding times during a desalination experiment. For example, for ACC-0.59, it is sufficient to have 10 min holding time for desalination at a molarity of 600 mM. However, at a lower concentration, this holding time can be shorter as the feedwater concentration decreases.

Cell voltage strongly influences performance stability in CDI. As shown in Figures 2F and 2G, electrochemical desalination with ACC-0.59 electrodes was conducted at cell voltages of 1.0, 1.2, and 1.4 V. Although increasing cell voltage usually enhances desalination capacity, it may yield accelerated electrode aging and performance degradation.[3] Performance degradation during cycling at cell voltages above the water stability window (1.23 V) leads to oxygen/hydrogen evolution, causing surface oxidation and the loss of microporosity.[47] As shown in Figures 2F and 2G, at 1.0 V polarization, the desalination capacity is 12 mg/g with a charge efficiency of 94%. The desalination performance remains stable, even after 200 cycles (12 mg/g, 91% at the 200th cycle). While increasing potential difference bias to 1.2 V, the initial desalination capacity of ACC-0.59 increased to 13.3 mg/g. Because of water splitting and surface oxidation under such cell voltage, the charge efficiency decreased to about 80% during the first 10 cycles. With further cycling, desalination capacity and charge efficiency decreased to 8 mg/g and 48%, respectively. At a cell voltage of 1.4 V, the initial desalination capacity reached 18.6 mg/g at a charge efficiency of about 80%, because of the stronger electric force. Increased water splitting and surface oxidation reactions reduce desalination performance to 3.1 mg/g and 13% after 200 cycles.

Molecular dynamics simulation of in-pore ion processes

To mechanistically understand capacitive deionization performance as a function of pore size, we performed MD simulations with a 600 mM NaCl aqueous electrolyte

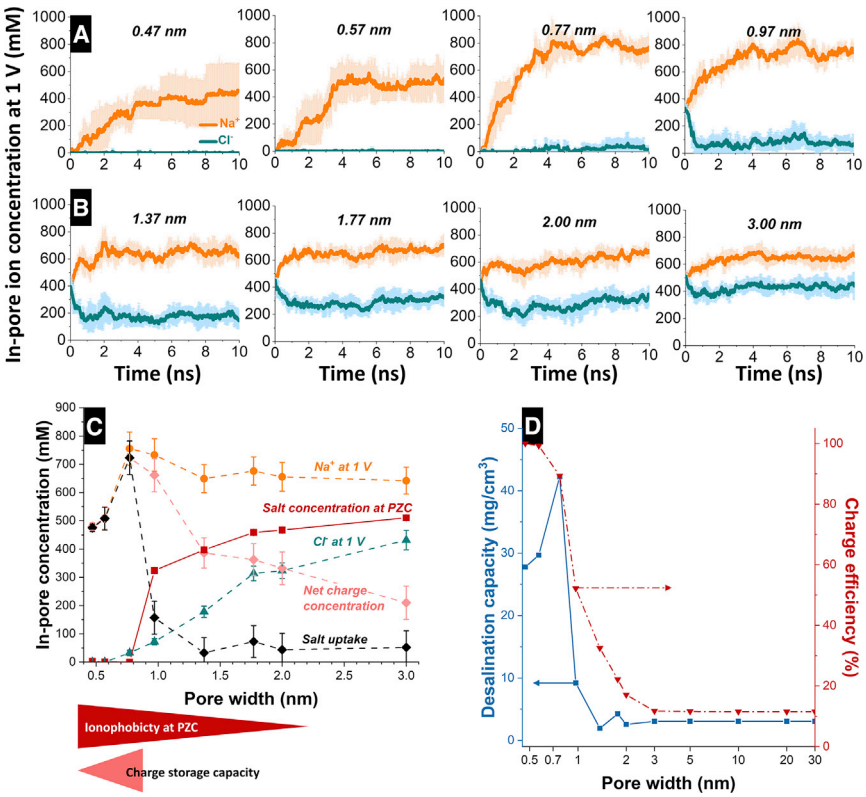

Figure 3. Molecular dynamics simulations of the dynamic change of in-pore ion species under 1 V cell voltage

(A) Numbers of Na^+ and Cl^- in pores of sub-nanometer sizes. Error bars were obtained from four simulations.

(B) Numbers of Na^+ and Cl^- in pores from 1 to 3 nm. Error bars were obtained from four simulations.

(C) Calculated in-pore Na^+ uptake and Cl^- release concentration, salt concentration at the potential of zero charge, net charge concentration, and salt uptake concentration. Values with error bars were obtained from the data of the last 2 ns from (A) and (B).

(D) Calculated desalination capacities and charge efficiencies in pores of different sizes. Time-dependent ion concentration evolution with error bars were obtained from four simulations.

under an electrode potential difference of 1 V. The MD simulation uses the constant potential method,[35] as also outlined in more detail in the Experimental procedures.

Time-dependent ion concentration development in negatively charged pores with different sizes are shown in Figures 3A and 3B (1 V cell voltage in 600 mM NaCl). At t = 0 ns, the Na^+ and Cl^- ion number in pores below 0.77 nm is almost zero. Hence, except for water molecules, pores smaller than the hydrated ion size remain empty in the uncharged state. During negative polarization, the concentration of Na^+ ions is increased over time, and Cl^- exclusion is impossible. Among all sub-nanometer pores, pores with size about 0.77 nm adsorb most additional counter-ions. As pore size increases to 0.97 nm, a significant number of Na^+ and Cl^- ions are already present at the PZC; during negative polarization, some Cl^- exclusion can be observed. As pore size increases from 1.37 to 3.0 nm, the number of ion pairs in the uncharged state increases. During negative polarization, the fraction of Cl^- exclusion increases relative to Na^+ adsorption.

Figure 3C shows the ion/salt concentration inside the pores at the end of the charging process in Figures 3A and 3B. The Na^+ uptake and Cl^- release

concentrations are the concentration changes between the charged and uncharged states. Salt uptake is calculated by subtracting the Cl^- ion release from Na^+ uptake. The in-pore Na^+ concentration minus the in-pore Cl^- concentration in the charged state corresponds to the net charge concentration (density). Below 0.77 nm, net charge concentration, Na^+ concentration, and salt uptake increase as pore size becomes larger. This aligns with the decreased energy demand for ion desolvation for larger pores. When pore size is larger than 0.77 nm, both cations and anions can enter the pore already at the PZC, and co-ion rejection becomes a limiting factor for salt uptake. As pore size increases further from 0.97 to 1.37 nm, Cl^- ion release during negative polarization becomes more pronounced because of increasing salt concentration at the PZC. Because of the limited capacitance (and hence ionic charge) of a given slit pore, increased Cl^- ion release leads to a decrease in Na^+ uptake. Consequently, total salt uptake decreases dramatically as pore size increases from 0.97 to 3 nm.

From an energy storage point of view, an increased net charge density is observed when pore size decreases from 3 to 0.77 nm, and it decreases when pore size decreases from 0.77 to 0.47 nm. In 2006, Chmiola et al.[48] described an anomalous capacitance increase at pore size less than 1 nm, which is associated with the distortion or (partial) loss of the solvation shell. The screening of the Coulomb repulsion of in-pore ions by the conductive pore walls allows an increased ion number to populate pores smaller than 1 nm.[49–51] The enhancement of the CDI capacity in the smallest pores found in this work goes beyond this anomalous capacitance effect and is related to the ionophobicity at the PZC. The counter-ion concentration slightly increases when pore size is decreased from 3 nm to about 0.77 nm. It decreases dramatically when pore size goes down further from 0.77 to 0.47 nm when ion desolvation is required during the charging process. On the other hand, a continuous decrease of in-pore co-ion concentration is observed when pore size is decreased. The capacitance increase (counter-ion concentration minus co-ion concentration) from 3 nm to about 0.77 nm is caused primarily by the changing number of in-pore co-ions rather than counter-ions.

Figure 3D shows the simulated charge efficiency and calculated desalination capacity of pores at different sizes. Smaller sub-nanometer pores have a much higher charge efficiency (close to 100%) due to the more pronounced ionophobicity, which increases as pore size decreases.[52] However, desalination capacity becomes lower at pore sizes below 0.77 nm, which is due to the higher desolvation energy for solvated ions to enter the smaller pores.[48] Desalination capacity reaches a maximum of 42 mg/cm^3 at 0.77 nm before it decreases significantly to 1.8 mg/cm^3 for larger pores. Above 3 nm, the in-pore salt concentration in the charged state and at the PZC remains constant. This implies that desalination capacity and charge efficiency approach constant values at a very low, non-zero level. Figure S3A compares the experimental desalination capacity data from our previous work[53] and the charge efficiency data from this work. The calculated desalination performance at different pore sizes for the porosity of ACC-0.59 is plotted in Figure S3B. Although the works show a similar trend, the finding of a pore size effect on desalination performance requires more reliable quantification, especially in seawater molar strength in which ionophobicity plays a vital role.

To better understand the effect of pore size on desalination at a molecular level, we modeled the double-layer structures and calculated the potential distributions in pores of different sizes under 1 V polarization (Figure 4). When pore size is smaller than 3 nm, the extension of the opposed electric double layers (EDLs) at the pore

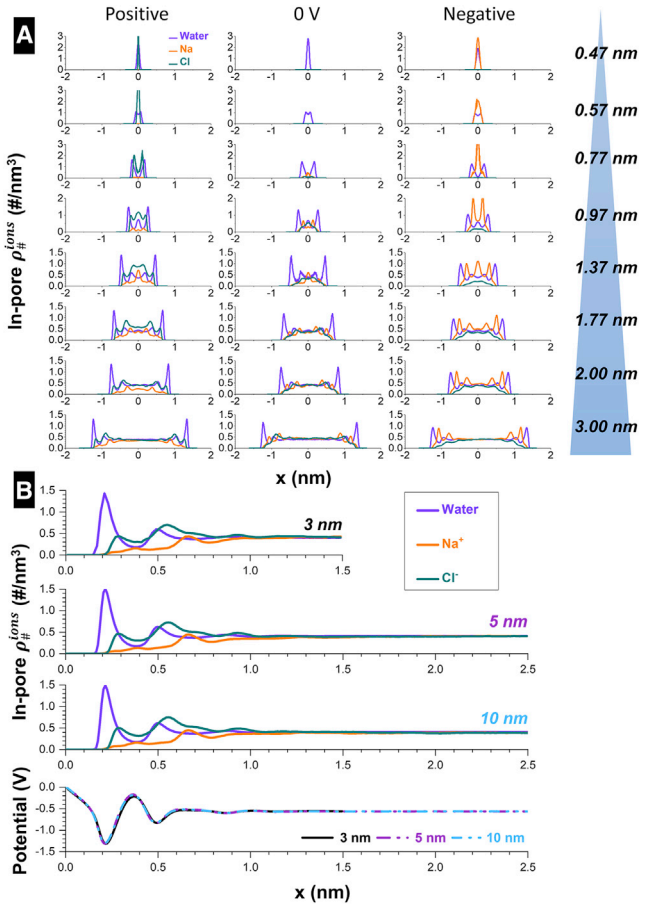

Figure 4. Simulated ion and water distributions in pores under positive polarization, point of zero charge, and negative polarizations

(A) Ion distributions in pores between 0.47 and 3 nm.

(B) Ion and water density distributions and potential distributions in pores between 3 and 10 nm, under positive polarization. X = 0 corresponds to the wall of the pores. For negative and positive polarization, the potential bias between both electrodes is 1 V. The number density of water is scaled by 1/80.

walls will overlap. This explains the stronger dependency of ion distributions in sub-nanometer pores (Figure 4A). In pores larger than 3 nm (Figure 4B), the EDL structure is well established and stabilized with little overlapping, and in the pore center, the ion concentration is nearly the same as the bulk ion concentration. Accordingly, the ion and potential distributions across EDLs are no longer dependent on the pore size.

The radial distribution functions (RDFs) and cumulative distribution functions (CDFs) between in-pore ions and their surrounding water molecules (Figure S4) indicate that the coordination number of water molecules of ions at 600 mM molar strength changes with pore size. The coordination number of in-pore Na^+ ions at negative polarization is smaller in ionophobic pores (<0.77 nm; see also Figure S5). This indicates that ion desolvation occurs mainly in ionophobic pores. Upon charging, the negative polarization causes the counter-ions to overcome the desolvation energy penalty so that Na^+ ions can enter the pore. Hence, the interplay between sub-nanometer pore smaller than the hydrated ion size and the high solvation energies of alkali metal ions in aqueous solution could explain ionophobicity and the high

desalination performance of ACC-0.59. Carbons below the hydrated ion size (Figure 3D) are ideal for high CDI performance: they are small enough to be ionophobic at the PZC but large enough to accommodate a large number of counter-ions (next to water molecules) upon charge.

On the basis of these findings and MD simulation results in Figure 3D, it is possible to calculate the capacitive seawater desalination performance of porous carbon electrodes (Data S1). With pore size distribution as input, and desalination performance as output, on the basis of Figure 3D, the pore volume-weighted desalination capacity and pores' charge efficiency at each pore size/volume are calculated by applying the interpolation relation between each simulated point. The total desalination performance of porous carbon electrodes can be predicted by adding up the desalination performance contributions of pores of different sizes. The predicted desalination capacity and charge efficiency value of ACC-0.59 are 10 mg/g and 87%, about 83% of the experimental calculated data (12 mg/g and 94%). The deviation is within the error of the MD simulation (26% at a pore size of 0.57 nm). Snapshots of MD models with different pore sizes are shown in Figure S6.

DISCUSSION

In this combined experimental and modeling work, carbon materials with sub-nanometer average pore sizes are investigated for their desalination application in both low and highly saline media. The pore size dependency of charge efficiency and desalination capacity allows calculation of desalination performance for carbons of specific pore size distributions. ACC-0.59, with an average pore size of about 0.6 nm, shows excellent desalination performance even at seawater-level molar strength. MD simulations explain this unexpectedly high performance to stem from the ionophobicity of pores smaller than 0.77 nm. As there are no ions present in the pores at the PZC, the counter-ion uptake upon charge and the desalination performance is large. Only upon charging, counter-ions strip off parts of their hydration shell and enter the sub-nanometer pores.

The desalination capacity of sub-nanometer pores shows a maximum at a pore size of 0.77 nm (42 mg/cm^3). Hence, the ideal CDI pore size corresponds to pores small enough to be ionophobic at the PZC yet large enough to take up a large number of counter-ions upon charging. The charge efficiency is shown to be nearly 100% for pores smaller than 0.57 nm, before it decreases significantly as pore size increases from 0.77 to 3 nm. The ability of sub-nanometer carbon pores to accomplish efficient desalination at the seawater concentration level dramatically enhances the practical application portfolio of CDI to overcome a niche application existence.

EXPERIMENTAL PROCEDURES

Resource availability

Lead contact

Further information and requests for resources and materials should be directed to, and will be fulfilled by, the lead contact, Volker Presser (volker.presser@leibniz-inm.de).

Materials availability

This study did not generate new unique materials.

Data and code availability

The datasets generated in this study are available from the lead contact on request.

Materials and reagents

NaCl (≥99%) was obtained from Sigma-Aldrich. ACC-0.59 and ACC-0.96 activated carbon cloths were obtained from Kynol. AC-1.39 was obtained from Kuraray. TiC powder was purchased from Sigma-Aldrich.

Carbon materials and characterizations

We used commercially available novolac-derived activated carbon cloth (Kynol ACC 5092-10 and Kynol ACC 507-20) with thicknesses of 600 and 250 μm as electrodes. The carbon cloth was used without adding any binder or conductive additives.

TiC-CDC was synthesized by annealing TiC powder at 400°C in dry chlorine gas for 3 h; then the sample was treated in hydrogen gas at 600°C for 2 h to remove residual chlorine species.[3] This sample is labeled CDC-0.57. Commercially available activated carbon YP-80F was used as received and is referred to as AC-1.39 in this paper.[48]

The AC-1.39 and CDC-0.57 electrodes were prepared by mixing the carbon particles with 10 mass% polytetrafluoroethylene (PTFE; Sigma-Aldrich) in ethanol. The obtained homogeneous carbon paste was rolled in an electric hot rolling press (MTI HR01; MTI Corporation) to have electrodes with homogeneous thickness (600 μm for AC-1.39 and 200 μm for CDC-0.57). Afterward, the electrodes were annealed at 120°C for 24 h in a vacuum furnace.

We conducted scanning electron microscopy for ACC-0.59 and ACC-0.96 using a Zeiss Gemini SEM 500 at 1 kV. The samples AC-1.39 and CDC-0.57 were characterized using a JEOL JSM 7500F field emission scanning electron microscope at 3 kV.

Data for the pore structure were adapted from our previous work.[47,54] In the previous work, argon gas sorption analysis was conducted using an Autosorb iQ system at a temperature of −186°C. The electrode sample was first degassed at 100 Pa and +200°C for 1 h and then heated to +300°C for 20 h to remove residual surface functional groups. The pore size distribution is obtained by applying quenched solid density functional theory using a slit-shaped pore kernel.[36]

The CHNS-O measurement was conducted to obtain element-specific chemical information of the carbon's functional groups. The amounts of H, C, and N were quantified using a Vario MICRO Cube (Elementar Analysensysteme) and heating up to +1,150°C at the combustion tube and +850°C at the reduction tube. The O content was quantified with an OXY cube elemental analyzer (Elementar Analysensysteme) at a pyrolysis temperature of +1450°C.

Desalination experiments

A symmetric full-cell configuration in batch mode was applied to test the desalination performance of the activated carbon material. In alignment with previous work,[43] the carbon cloth was cut into a pair of round disks 30 mm in diameter. A fixed 3 mm distance is set by the thickness of the middle channel with six glass fiber separators (Millipore) and four pieces of polyethylene terephthalate mesh placed between the two electrodes. The feedwater is pumped at a flow rate of 2.5 mL/min to flow between the electrodes. The feedwater is cycled back to a 10 L reservoir to minimize the concentration fluctuation between charging and discharging processes.

At the CDI cell outlet, the water's ion concentration and pH change were recorded using pH and conductivity sensors (Metrohm 856 conductivity, Metrohm 867 pH Module). A Bio-Logic VSP-300 system was used to determine the electrochemical performance of the CDI cell. Galvanostatic charging and discharging were performed at a specific current of 0.1 A/g between 0 and +1, +1.2, and +1.4 V cell voltages with a holding time of 20 min.

Desalination capacity was determined using Equation 1:

$$DC = \left(v\frac{M_{salt}}{M_{tot}}\right)\int (c_t - c_0)dt\,, \qquad \text{(Equation 1)}$$

where M_{salt} is the molar mass of the salt, M_{tot} is the total mass of the two electrodes, v is the flow rate, and c_0 and c_t are the initial outlet salt concentration and concentrate of the feedwater at time t, respectively.

Charge efficiency was calculated according to Equation 2:

$$CE(\%) = \frac{F \times DC_{mol}}{M_{salt} \times Q} \times 100\%\,, \qquad \text{(Equation 2)}$$

where F is the Faraday constant (26,801 mAh/mol), DC_{mol} is the desalination capacity from Equation 1, and Q is the average of total charge (normalized to the total electrode mass, mAh/g) stored/released during the desalination/recovering process.

The energy consumption of the CDI process in units of kT/ion (where T = 298 K and k_B is the Boltzmann constant) is calculated by dividing the capacitive energy stored by the removed number of ions (Equation 3).

$$Energy\ consumption\left(\frac{kT}{ion}\right) = \frac{3600}{k_B T}\frac{1}{N_A}\frac{Q_{charge} * U}{n_{removed}}\,, \qquad \text{(Equation 3)}$$

where U is the cell voltage (V), Q_{charge} is the charge (Ah) stored during the desalination process, $n_{removed}$ is the amount of salt removed (mol), and N_A is the Avogadro constant.

Molecular dynamics simulations

The molecular dynamics simulation system consists of two slit-shaped pore electrodes immersed in 600 mM NaCl aqueous solution. Three layers of graphene sheets were used to model the walls of the electrode pore, and pore sizes were varied from 0.47 to 10 nm to cover a broad range of pore sizes in practical nanoporous carbon electrodes. The pore length was set to 6.33 nm to ensure that the edge effect of the electrode was not significant.[36] Force fields for electrodes and aqueous NaCl electrolytes are from Cornell et al.[55] and Smith and Dang,[56] and the SPC/E model[57] was chosen for the water molecules. The modified MD simulation software on the basis of GROMACS-4.6.7[56] was used for our simulation. To simulate the capacitive deionization process, a constant potential difference was applied between the two electrodes.[58] The MD simulation was performed in an isothermal and equal-volume ensemble (NVT) using the V-Resale temperature control method with a time step of 2 fs. The long-range electrostatic interactions are calculated using particle-mesh Ewald (PME) algorithm. The Fourier mesh spacing in reciprocal space is 0.1 nm, and the interpolation method is B-spline interpolation of order four. A cut-off of 1.2 nm was used to calculate the short-range electrostatic interactions and van der Waals interactions. The system was first simulated at 800 K for 2 ns, then cooled to 298 K after a linear annealing process of 5 ns, and then run at 298 K for 20 ns to achieve initial equilibrium. Next, a constant potential difference between the two electrodes was applied to simulate the

desalination process. Each group was simulated four times with different initial configurations to obtain reliable results from the simulation.

SUPPLEMENTAL INFORMATION

Supplemental information can be found online at https://doi.org/10.1016/j.xcrp.2021.100689.

ACKNOWLEDGMENTS

We thank Eduard Arzt (INM) for his continuing support. We thank Andrea Jung and Tamara Winter (INM) for support with CHNS-O measurements and SEM characterizations. Y.Z. and V.P. acknowledge support for the MERLIN project from RAG-Stiftung; RAG-Stiftung generates long-term momentum for the transformation of the regions along the Ruhr and Saar rivers and in Ibbenbüren. H.J. and G.F. acknowledge support from the National Natural Science Foundation of China (51836003) and the Program for HUST Academic Frontier Youth Team and also thank Beijing PARATERA Tech Co., Ltd., for providing high-performance computing (HPC) resources to accomplish simulations in this work. This project has received funding from the European Union's Horizon 2020 research and innovation programme under the Marie Skłodowska-Curie grant agreement No. 894042.

AUTHOR CONTRIBUTIONS

Conceptualization, Writing – Original Draft, Investigation, Visualization, and Data Curation, Y.Z.; Writing – Review & Editing, Visualization, Data Curation, and Validation, C.P.; Software, Methodology, Writing – Review & Editing, Visualization, and Data Curation, H.J.; Data Curation, Y.L.; Software, Methodology, Conceptualization, Supervision, Writing – Review & Editing, Project Administration, and Funding Acquisition, G.F.; Conceptualization, Supervision, Writing – Review & Editing, Project Administration, and Funding Acquisition, V.P.

DECLARATION OF INTERESTS

The authors declare no competing interests.

Received: August 25, 2021
Revised: November 3, 2021
Accepted: November 22, 2021
Published: December 13, 2021

REFERENCES

1. Shannon, M.A., Bohn, P.W., Elimelech, M., Georgiadis, J.G., Mariñas, B.J., and Mayes, A.M. (2008). Science and technology for water purification in the coming decades. Nature *452*, 301–310.

2. Humplik, T., Lee, J., O'Hern, S.C., Fellman, B.A., Baig, M.A., Hassan, S.F., Atieh, M.A., Rahman, F., Laoui, T., Karnik, R., and Wang, E.N. (2011). Nanostructured materials for water desalination. Nanotechnology *22*, 292001.

3. Porada, S., Borchardt, L., Oschatz, M., Bryjak, M., Atchison, J.S., Keesman, K.J., Kaskel, S., Biesheuvel, P.M., and Presser, V. (2013). Direct prediction of the desalination performance of porous carbon electrodes for capacitive deionization. Energy Environ. Sci. *6*, 3700–3712.

4. Miller, J.E. (2003). Review of water resources and desalination technologies (Albuquerque, NM: Sandia National Laboratories). https://www.osti.gov/servlets/purl/809106/.

5. Janowska, K., Boffa, V., Jørgensen, M.K., Quist-Jensen, C.A., Hubac, F., Deganello, F., Coelho, F.E.B., and Magnacca, G. (2020). Thermocatalytic membrane distillation for clean water production. npj Clean Water *3*, 34.

6. Ricceri, F., Giagnorio, M., Farinelli, G., Blandini, G., Minella, M., Vione, D., and Tiraferri, A. (2019). Desalination of produced water by membrane distillation: Effect of the feed components and of a pre-treatment by fenton oxidation. Sci. Rep. *9*, 14964.

7. Yao, Y., Zhang, P., Jiang, C., DuChanois, R.M., Zhang, X., and Elimelech, M. (2021). High performance polyester reverse osmosis desalination membrane with chlorine resistance. Nat. Sustain. *4*, 138–146.

8. Inukai, S., Cruz-Silva, R., Ortiz-Medina, J., Morelos-Gomez, A., Takeuchi, K., Hayashi, T., Tanioka, A., Araki, T., Tejima, S., Noguchi, T., et al. (2015). High-performance multi-functional reverse osmosis membranes obtained by carbon nanotube·polyamide nanocomposite. Sci. Rep. *5*, 13562.

9. Uliana, A.A., Bui, N.T., Kamcev, J., Taylor, M.K., Urban, J.J., and Long, J.R. (2021). Ion-capture electrodialysis using multifunctional adsorptive membranes. Science *372*, 296–299.

10. Zhao, R., Porada, S., Biesheuvel, P.M., and van der Wal, A. (2013). Energy consumption in membrane capacitive deionization for different

water recoveries and flow rates, and comparison with reverse osmosis. Desalination *330*, 35–41.

11. Pasta, M., Wessells, C.D., Cui, Y., and La Mantia, F. (2012). A desalination battery. Nano Lett. *12*, 839–843.

12. Biesheuvel, P.M., Porada, S., Levi, M., and Bazant, M.Z. (2014). Attractive forces in microporous carbon electrodes for capacitive deionization. J. Solid State Electrochem. *18*, 1365–1376.

13. Elimelech, M., and Phillip, W.A. (2011). The future of seawater desalination: energy, technology, and the environment. Science *333*, 712–717.

14. Anderson, M.A., Cudero, A.L., and Palma, J. (2010). Capacitive deionization as an electrochemical means of saving energy and delivering clean water. Comparison to present desalination practices: will it compete? Electrochim. Acta *55*, 3845–3856.

15. Porada, S., Zhao, R., van der Wal, A., Presser, V., and Biesheuvel, P.M. (2013). Review on the science and technology of water desalination by capacitive deionization. Prog. Mater. Sci. *58*, 1388–1442.

16. Bi, S., Zhang, Y., Cervini, L., Mo, T., Griffin, J.M., Presser, V., and Feng, G. (2020). Permselective ion electrosorption of subnanometer pores at high molar strength enables capacitive deionization of saline water. Sustain. Energy Fuels *4*, 1285–1295.

17. Suss, M.E., Porada, S., Sun, X., Biesheuvel, P.M., Yoon, J., and Presser, V. (2015). Water desalination via capacitive deionization: what is it and what can we expect from it? Energy Environ. Sci. *8*, 2296–2319.

18. Porada, S., Weinstein, L., Dash, R., van der Wal, A., Bryjak, M., Gogotsi, Y., and Biesheuvel, P.M. (2012). Water desalination using capacitive deionization with microporous carbon electrodes. ACS Appl. Mater. Interfaces *4*, 1194–1199.

19. Shi, W., Li, H., Cao, X., Leong, Z.Y., Zhang, J., Chen, T., Zhang, H., and Yang, H.Y. (2016). Ultrahigh performance of novel capacitive deionization electrodes based on a three-dimensional graphene architecture with nanopores. Sci. Rep. *6*, 18966.

20. Srimuk, P., Su, X., Yoon, J., Aurbach, D., and Presser, V. (2020). Charge-transfer materials for electrochemical water desalination, ion separation and the recovery of elements. Nat. Rev. Mater. *5*, 517–538.

21. Prehal, C., Weingarth, D., Perre, E., Lechner, R.T., Amenitsch, H., Paris, O., and Presser, V. (2015). Tracking the structural arrangement of ions in carbon supercapacitor nanopores using in situ small-angle X-ray scattering. Energy Environ. Sci. *8*, 1725–1735.

22. Biesheuvel, P.M., and van der Wal, A. (2010). Membrane capacitive deionization. J. Membr. Sci. *346*, 256–262.

23. Zhang, Y., Srimuk, P., Aslan, M., Gallei, M., and Presser, V. (2020). Polymer ion-exchange membranes for capacitive deionization of aqueous media with low and high salt concentration. Desalination *479*, 114331.

24. Tang, K., Kim, Y.-h., Chang, J., Mayes, R.T., Gabitto, J., Yiacoumi, S., and Tsouris, C. (2019). Seawater desalination by over-potential membrane capacitive deionization: opportunities and hurdles. Chem. Eng. J. *357*, 103–111.

25. Chen, F., Huang, Y., Guo, L., Sun, L., Wang, Y., and Yang, H.Y. (2017). Dual-ions electrochemical deionization: a desalination generator. Energy Environ. Sci. *10*, 2081–2089.

26. Smith, K.C., and Dmello, R. (2016). Na-ion desalination (NID) enabled by Na-blocking membranes and symmetric Na-intercalation: porous-electrode modeling. J. Electrochem. Soc. *163*, A530–A539.

27. Porada, S., Shrivastava, A., Bukowska, P., Biesheuvel, P.M., and Smith, K.C. (2017). Nickel hexacyanoferrate electrodes for continuous cation intercalation desalination of brackish water. Electrochim. Acta *255*, 369–378.

28. Srimuk, P., Kaasik, F., Krüner, B., Tolosa, A., Fleischmann, S., Jäckel, N., Tekeli, M.C., Aslan, M., Suss, M.E., and Presser, V. (2016). MXene as a novel intercalation-type pseudocapacitive cathode and anode for capacitive deionization. J. Mater. Chem. A Mater. Energy Sustain. *4*, 18265–18271.

29. Zhang, Q., Aung, S.H., Oo, T.Z., and Chen, F. (2020). Continuous electrochemical deionization by utilizing the catalytic redox effect of environmentally friendly riboflavin-5′-phosphate sodium. Mater. Today Commun. *23*, 100921.

30. Cai, P.F., Su, C.J., Chang, W.T., Chang, F.C., Peng, C.Y., Sun, I.W., Wei, Y.L., Jou, C.J., and Wang, H.P. (2014). Capacitive deionization of seawater effected by nano Ag and Ag@C on graphene. Mar. Pollut. Bull. *85*, 733–737.

31. Nam, D.-H., and Choi, K.-S. (2017). Bismuth as a new chloride-storage electrode enabling the construction of a practical high capacity desalination battery. J. Am. Chem. Soc. *139*, 11055–11063.

32. Arnold, S., Wang, L., Budak, Ö., Aslan, M., Srimuk, P., and Presser, V. (2021). Antimony alloying electrode for high-performance sodium removal: how to use a battery material not stable in aqueous media for saline water remediation. J. Mater. Chem. A Mater. Energy Sustain. *9*, 585–596.

33. Zhang, Y., Wang, L., and Presser, V. (2021). Electrocatalytic fuel cell desalination for continuous energy and freshwater generation. Cell Reports Physical Science *2*, 100416.

34. Atlas, I., Khalla, S.A., and Suss, M.E. (2020). Thermodynamic energy efficiency of electrochemical systems performing simultaneous water desalination and electricity generation. J. Electrochem. Soc. *167*, 134517.

35. Uwayid, R., Seraphim, N.M., Guyes, E.N., Eisenberg, D., and Suss, M.E. (2021). Characterizing and mitigating the degradation of oxidized cathodes during capacitive deionization cycling. Carbon *173*, 1105–1114.

36. Kim, C., Srimuk, P., Lee, J., Fleischmann, S., Aslan, M., and Presser, V. (2017). Influence of pore structure and cell voltage of activated carbon cloth as a versatile electrode material for capacitive deionization. Carbon *122*, 329–335.

37. Partheniades, E. (2009). Forces between clay particles and the process of flocculation. In Cohesive Sediments in Open Channels, E. Partheniades, ed. (Boston: Butterworth-Heinemann), pp. 47–88.

38. Levy, A., de Souza, J.P., and Bazant, M.Z. (2020). Breakdown of electroneutrality in nanopores. J. Colloid Interface Sci. *579*, 162–176.

39. Hess, B., Kutzner, C., van der Spoel, D., and Lindahl, E. (2008). GROMACS 4: algorithms for highly efficient, load-balanced, and scalable molecular simulation. J. Chem. Theory Comput. *4*, 435–447.

40. Reed, S.K., Madden, P.A., and Papadopoulos, A. (2008). Electrochemical charge transfer at a metallic electrode: a simulation study. J. Chem. Phys. *128*, 124701.

41. Feng, X., Dementev, N., Feng, W., Vidic, R., and Borguet, E. (2006). Detection of low concentration oxygen containing functional groups on activated carbon fiber surfaces through fluorescent labeling. Carbon *44*, 1203–1209.

42. Prehal, C., Koczwara, C., Amenitsch, H., Presser, V., and Paris, O. (2018). Salt concentration and charging velocity determine ion charge storage mechanism in nanoporous supercapacitors. Nat. Commun. *9*, 4145.

43. Zhang, Y., Srimuk, P., Husmann, S., Chen, M., Feng, G., and Presser, V. (2019). Effect of pore size on the ion electrosorption and hydrogen/deuterium electrosorption using sodium chloride in H_2O and D_2O. J. Electrochem. Soc. *166*, A4158–A4167.

44. Jäckel, N., Weingarth, D., Schreiber, A., Krüner, B., Zeiger, M., Tolosa, A., Aslan, M., and Presser, V. (2016). Performance evaluation of conductive additives for activated carbon supercapacitors in organic electrolyte. Electrochim. Acta *191*, 284–298.

45. Dash, R., Chmiola, J., Yushin, G., Gogotsi, Y., Laudisio, G., Singer, J., Fischer, J., and Kucheyev, S. (2006). Titanium carbide derived nanoporous carbon for energy-related applications. Carbon *44*, 2489–2497.

46. Karamanova, B., Stoyanova, A., Shipochka, M., Girginov, C., and Stoyanova, R. (2019). On the cycling stability of biomass-derived carbons as electrodes in supercapacitors. J. Alloys Compd. *803*, 882–890.

47. Presser, V., Heon, M., and Gogotsi, Y. (2011). Carbide-derived carbons—from porous networks to nanotubes and graphene. Adv. Funct. Mater. *21*, 810–833.

48. Chmiola, J., Yushin, G., Gogotsi, Y., Portet, C., Simon, P., and Taberna, P.L. (2006). Anomalous increase in carbon capacitance at pore sizes less than 1 nanometer. Science *313*, 1760–1763.

49. Merlet, C., Péan, C., Rotenberg, B., Madden, P.A., Daffos, B., Taberna, P.L., Simon, P., and Salanne, M. (2013). Highly confined ions store charge more efficiently in supercapacitors. Nat. Commun. *4*, 2701.

50. Kondrat, S., and Kornyshev, A. (2011). Superionic state in double-layer capacitors with nanoporous electrodes. J. Phys. Condens. Matter *23*, 022201.

51. Prehal, C., Koczwara, C., Jäckel, N., Schreiber, A., Burian, M., Amenitsch, H., Hartmann, M.A., Presser, V., and Paris, O. (2017). Quantification of ion confinement and desolvation in nanoporous carbon supercapacitors with modelling and in situ X-ray scattering. Nat. Energy *2*, 16215.

52. Merlet, C., Rotenberg, B., Madden, P.A., Taberna, P.-L., Simon, P., Gogotsi, Y., and Salanne, M. (2012). On the molecular origin of supercapacitance in nanoporous carbon electrodes. Nat. Mater. *11*, 306–310.

53. Porada, S., Schipper, F., Aslan, M., Antonietti, M., Presser, V., and Fellinger, T.-P. (2015). Capacitive deionization using biomass-based microporous salt-templated heteroatom-doped carbons. ChemSusChem *8*, 1867–1874.

54. Aslan, M., Zeiger, M., Jäckel, N., Grobelsek, I., Weingarth, D., and Presser, V. (2016). Improved capacitive deionization performance of mixed hydrophobic/hydrophilic activated carbon electrodes. J. Phys. Condens. Matter *28*, 114003.

55. Cornell, W.D., Cieplak, P., Bayly, C.I., Gould, I.R., Merz, K.M., Ferguson, D.M., Spellmeyer, D.C., Fox, T., Caldwell, J.W., and Kollman, P.A. (1995). A second generation force field for the simulation of proteins, nucleic acids, and organic molecules. J. Am. Chem. Soc. *117*, 5179–5197.

56. Smith, D.E., and Dang, L.X. (1994). Computer simulations of NaCl association in polarizable water. J. Chem. Phys. *100*, 3757–3766.

57. Feng, G., and Cummings, P.T. (2011). Supercapacitor capacitance exhibits oscillatory behavior as a function of nanopore size. J. Phys. Chem. Lett. *2*, 2859–2864.

58. Berendsen, H.J.C., Grigera, J.R., and Straatsma, T.P. (1987). The missing term in effective pair potentials. J. Phys. Chem. *91*, 6269–6271.